Applied Physics A (2018) 124:372
https://doi.org/10.1007/s00339-018-1790-3

Applied Physics A
Materials Science & Processing

Simulation of photobioreaction for hydrogen production in membrane bioreactor with an optical fiber

Yanxia Yang[1,2] · Jing Li[3]

Received: 25 November 2017 / Accepted: 12 April 2018 / Published online: 16 April 2018

Abstract
A generalized lattice Boltzmann (LB) model for porous media is adopted to simulate the hydrodynamics and mass transport combined with biodegradation in membrane bioreactor with a circular optical fiber. The LB model is coupled with a multi-block scheme, as well as non-equilibrium extrapolation method for boundary condition treatment. The effect of porosity and permeability (represented by Darcy number *Da*) of biofilm on flow and concentration fields are investigated. The performance of biodegradation is evaluated by substrate consumption efficiency. Higher porosity and permeability of biofilm facilitate mass transport of substance and enhance the metabolic activity of bacteria in biofilm, which results in the optimal biodegradation performance is obtained under the condition of $Da = 0.001$ and $\varepsilon = 0.3$. For further increasing of these parameters, the substrate consumption efficiency decreases due to the inhibition effect of substrate and shorter hydraulic retention time. Furthermore, the LB results coincide with experimental results, demonstrating that the LB model for porous media is available to optimize the membrane bioreactor for efficient biodegradation.

1 Introduction

Due to diversified human activities and increasing industrialization, the escalating wastewater discharges with kinds of pollutants have badly destroyed human health and eco-environment. This severe situation has promoted the development of novel processes for wastewater treatment, including chemical and biological processes [1–3]. Recently, biological treatment has been proven as an efficient wastewater treatment technology and widely used in the processes of city sewage and industrial waste treatment. The cell immobilized techniques, such as biofilm and gel-granules immobilized technologies [1, 4] have been applied in the bioreactor to elevate biomass concentration. Noteworthily, biomembranes can exhibit greater resistance to toxic shocks and retention of slow-growing microorganisms, which makes biofilm beneficial wastewater treatment strategies, and achieves efficient removal of a variety of contaminants [5]. Especially, photosynthetic bacteria (PSB) has significant superiority in degrading the organic compounds in wastewater by utilizing solar energy and simultaneously generating hydrogen energy, which is considered as a promising candidate due to its advantages of high energy content, high stability of combustion, cleanness and high efficiency [6]. Therefore, biomembrane wastewater treatment can accomplish energy conservation and emissions reduction.

Biofilm is aggregates of microorganisms suspended in a matrix of extracellular polymeric substances (EPS), which is driven by Brownian movement and fluid motion and then attached to carrier's surface, finally forming a layer of biofilm [1]. The biomembrane technique multiplies the PSB as well as enhances the resistance to toxic substance and fluid flush, and thereby improves the stability of bioreactor and degradation performance. Consequently, biofilm is the foundation of biological membrane processing for wastewater treatment systems [1], and the characteristics of biofilm directly determine the mass transportation and biodegradation in the bioreactor. The structure of biofilm has been proven to be porous media, and then the degradation process can be considered as a bioreaction in porous media. Recently, numerous bioreactors and experiments have been proposed and implemented with the aim of improving the

✉ Yanxia Yang
yangyanxia@tyut.edu.cn

1 College of Electrical and Power Engineering, Taiyuan University of Technology, Taiyuan 030024, Shanxi, China

2 Key Laboratory of Low-grade Energy Utilization Technologies and Systems, Ministry of Education of China, Chongqing University, Chongqing 400044, China

3 College of Environmental Science and Engineering, Taiyuan University of Technology, Taiyuan 030024, Shanxi, China

stability of reactors and performance of hydrogen production. For example, the effects of bacterium resource and operating condition have been investigated [7–9]. Except experimental studies, many theoretical studies have been carried out, and some numerical models have been established to investigate the bioreaction [10–12] and two-phase flow transport in the bioreactor [4, 13]. Noteworthily, these numerical models are generally based on macro-scale, and require to solve the partial difference equations for complex system. Moreover, they are still quite limited in obtaining the detailed information of fluid flow and mass transport in biofilm, and also have difficulties in treating complex geometry. Therefore, it is necessary to carry out a further numerical study on the flow and mass transport in the bioreactor to overcome the limitations.

Recently, lattice Boltzmann method (LBM) has been proposed as an alternative and promising numerical algorithm. Unlike conventional numerical methods based on macroscopic continuum equations, the LBM is a mesoscopic approach that incorporates the essential physics of microscopic or mesoscopic process [14, 15]. Lattice Boltzmann models are based on microscopic kinetic equation for the particle distribution function, and the macroscopic quantities are then obtained through moment integrations of the distribution function [16] which can lead to the macroscopic equations by means of a Chapman–Enskog expansion [17, 18]. Lattice Boltzmann models retain the essence of the physical processes, and thus conserve the simplicity and intuitive nature which is required for adding new components in a problem or considering more complex phenomena. Furthermore, LBM has the most distinguished advantages, such as the simplicity of algorithm, the flexibility for complex geometries and parallel computing [19, 20]. Recently, kinds of lattice Boltzmann models have been developed for different science engineering problems, and successfully applied in multicomponent and multiphase [21–25], flow in porous media [26–30] and reaction flow [31–33]. Therefore, the lattice Boltzmann method can be adopted to investigate directly the local flow and mass transfer associated with biodegradation in the photobioreactor.

In present study, a generalized lattice Boltzmann model for porous media at representative elementary volume REV scale [34] is applied to simulate the bioreaction combined with fluid flow and mass transfer in a photobioreactor, where a layer of uniform PSB biofilm is attached on a circular optical fiber. Different from most previous numerical simulations, which are based on the discretizations of certain semiempirical models using some standard conventional techniques [35], the generalized lattice Boltzmann model takes into account of the linear and nonlinear matrix drag components as well as the inertial and viscous forces, overcoming the limitations of the Darcy or Brinkman model for flows in porous media [34]. The solution fluid in the bioreactor is considered as incompressible fluid, and the model has capabilities to simulate the porous flow for incompressible fluid over a wide range and to treat a variable porosity without invoking any additional boundary conditions [34]. In the simulation, a multi-block strategy [36] is coupled with the lattice Boltzmann model to improve the computational efficiency and accuracy. The effects of porosity and permeability of biofilm on flow and concentration fields as well as substrate consumption efficiency are investigated to improve the performance of bioreactor.

2 Lattice Boltzmann model

2.1 Hydrodynamic equations

The lattice Boltzmann model for incompressible fluid flow in porous media at REV scale [34] is used to describe the velocity field, and the density distribution function f_i is given by,

$$f_i(\mathbf{x}+\mathbf{e}_i\delta_t, t+\delta_t) - f_i(\mathbf{x},t) = -\tau_v^{-1}\left(f_i(\mathbf{x},t) - f_i^{\mathrm{eq}}(\mathbf{x},t)\right) + \delta_t F_i, \tag{1}$$

where F_i represents force term and defined as [34],

$$F_i = \omega_i\rho\left(1-\frac{1}{2\tau}\right)\left[\frac{\mathbf{e}_i\cdot\mathbf{F}}{c_s^2} + \frac{\mathbf{uF}:(\mathbf{e}_i\mathbf{e}_i - c_s^2\mathbf{I})}{\varepsilon c_s^4}\right], \tag{2}$$

where δ_t is time step and τ_v is the non-dimensional relaxation time. $\mathbf{e}_i$ is the particle velocity vector and ω_i is the weight coefficient. $f_i^{\mathrm{eq}}(\mathbf{x},t)$ is corresponding equilibrium distribution function at position $\mathbf{x}$ and time t. In D2Q9 model, $f_i^{\mathrm{eq}}(\mathbf{x},t)$ is defined as,

$$f_i^{\mathrm{eq}} = \omega_i\rho\left[1+\frac{\mathbf{e}_i\cdot\mathbf{u}}{c_s^2} + \frac{\mathbf{uu}:(\mathbf{e}_i\mathbf{e}_i - c_s^2\mathbf{I})}{2\varepsilon c_s^4}\right] \quad i=0,1,\ldots,8, \tag{3}$$

where $\mathbf{e}_i$ and ω_i are given by

$$\mathrm{e} = c\begin{bmatrix}0&1&0&-1&0&1&-1&-1&1\\0&0&1&0&-1&1&1&-1&-1\end{bmatrix} \text{and}$$

$$\omega_i = \begin{cases}4/9, i=0\\1/9, i=1-4\\1/36, i=5-8\end{cases}, \text{ where } c_s \text{ is the sound speed}$$

$c_s = c/\sqrt{3}$, and c is the lattice speed, $c = \delta_x/\delta_t$, with the space step δ_x.

The macroscopic fluid volume-averaged density and velocity can be calculated as [34],

$$\rho = \sum f_i, \tag{4}$$

$$\mathbf{u} = \frac{\mathbf{v}}{a_0 + \sqrt{a_0^2 + a_1|\mathbf{v}|}}, \tag{5}$$

where the temporal velocity is given by $\mathbf{v} = \sum \mathbf{e}_i f_i/\rho + \frac{\delta_t}{2}\varepsilon\mathbf{G}$, with two parameters of $a_0 = \frac{1}{2}\left(1 + \varepsilon\frac{\delta_t}{2}\frac{\nu}{K}\right)$ and $a_1 = \varepsilon\frac{\delta_t}{2}\frac{F_\varepsilon}{\sqrt{K}}$.

In the limit of small Mach number and Chapman–Enskog expansion, the following macroscopic equations can be derived from the above lattice Boltzmann equations,

$$\frac{\partial(\rho\mathbf{u})}{\partial t} + \nabla\cdot(\rho\mathbf{u}) = 0, \tag{6}$$

$$\frac{\partial(\rho\mathbf{u}\mathbf{u})}{\partial t} + \nabla\cdot\left(\frac{\rho\mathbf{u}\mathbf{u}}{\varepsilon}\right) = -\nabla p + \nabla\cdot\left[\rho\nu_e(\nabla\mathbf{u} + \mathbf{u}\nabla)\right] + \mathbf{F}, \tag{7}$$

where the pressure is $p = c_s^2\rho/\varepsilon$ and the kinematical viscosity is $\nu_e = c_s^2(\tau_\nu - 0.5)\delta_t$. F is the total external body force and given by [34]

$$\mathbf{F} = -\frac{\varepsilon\nu}{K}\mathbf{u} - \frac{\varepsilon F_\varepsilon}{\sqrt{K}}|\mathbf{u}|\mathbf{u} + \varepsilon\mathbf{G}. \tag{8}$$

In Eq. (8), $\mathbf{G}$ is the external body force. The first and the second terms in the right hand side are the Darcy's term and Forcheimer's term. The permeability K and geometric function F_ε of porous medium are related to the porosity ε, which are based on Ergun's experimental investigations and can be described by $K = \frac{\varepsilon^3 d_p^2}{150(1-\varepsilon)^2}$ and $F_\varepsilon = \frac{1.75}{\sqrt{150\varepsilon^3}}$ [37, 38], and the diameter of solid particle d_p in porous medium varies with the change of porosity to maintain the same value of permeability for a given Darcy number.

2.2 Mass transfer equations

The LB model proposed by Sullivan [33] is adopted for mass transfer. In this model, mass transport is decoupled from hydrodynamic simulation, which enables the hydrodynamic relaxation time τ_ν to be tuned separately from mass transfer relaxation τ_σ. There are also some modifications in the model that the use of a rest fraction J_0 and a reduction of discrete directions without loss of accuracy. The concentration distribution function $g_{i,\sigma}$ for σ-species is used for concentration field, and expressed as [33],

$$\begin{aligned} &g_{i,\sigma}(\mathbf{x} + \mathbf{e}_i\delta_t, t + \delta_t) - g_{i,\sigma}(\mathbf{x}, t) \\ &\quad = -\tau_\sigma^{-1}\left(g_{i,\sigma}(\mathbf{x}, t) - g_{i,\sigma}^{\mathrm{eq}}(\mathbf{x}, t)\right) + J_{i,\sigma}\delta_t r_\sigma, \end{aligned} \tag{9}$$

where τ_σ is the non-dimensional relaxation time corresponding to $g_{i,\sigma}$, and r_σ is the reaction source.

In this model, the discrete directions reduce from 9 to 5 without loss of accuracy, and the corresponding equilibrium distribution function $g_{i,\sigma}^{\mathrm{eq}}$ is given as [33],

$$g_{i,\sigma}^{\mathrm{eq}} = c_\sigma\left(J_{i,\sigma} + K_i\frac{\mathbf{e}_i\cdot\mathbf{u}}{c^2}\right) \quad i = 0, 1, \ldots, 4, \tag{10}$$

where $J_{i,\sigma}$ and K_i are constants, $K_i = 1/2$, $J_{0,\sigma} = J_0$, $J_{i,\sigma} = (1 - J_0)/4$, where J_0 can be tuned between 0 to 1.

The macroscopic concentration of σ-species can be calculated by,

$$c_\sigma(\mathbf{x}, t) = \sum_i g_{i,\sigma}(\mathbf{x}, t). \tag{11}$$

Similarly, the macroscopic mass transfer equations can be obtained by the above lattice Boltzmann equations for concentration field,

$$\frac{\partial c_\sigma}{\partial t} + \mathbf{u}\nabla c_\sigma - D_\sigma\nabla^2 c_\sigma = r_\sigma, \tag{12}$$

where the diffusivity is evaluated by $D_\sigma = \delta_t c^2 C_Q(1 - J_0)\left(\tau_\sigma - \frac{1}{2}\right)$ with $C_Q = 1/2$.

2.3 Multi-block strategy for LBM

In order to obtain more detailed and accurate results, a multi-block strategy is adopted and coupled with the lattice Boltzmann model. For the multi-block scheme proposed by Yu et al. the fine block is not entirely overlapped by the coarse block to improve the accuracy and computational efficiency, only uses partially overlapped blocks at the interfacial lattices for coupling to satisfy the continuity of mass, momentum and stresses across the interface [36].

A two-block system in Fig. 1a is used to illustrate the scheme for particle distribution exchange at the interface. The ratio of the lattice space between the two blocks is $m = \delta_{x,c}/\delta_{x,f}$, where $\delta_{x,c}$ and $\delta_{x,f}$ are lattice space of coarse grid and fine grid, denoted by subscripts "c" and "f", respectively.

In order to keep a consistent viscosity, the relaxation times for two blocks have the relationship:

$$\tau_f = \frac{1}{2} + m\left(\tau_c - \frac{1}{2}\right). \tag{13}$$

When transferring the information from fine block to coarse block, the post-collision distribution function at nodes "▲" can be obtained by [36]

$$f_i^{+,c} = f_i^{\mathrm{eq},f} + m\frac{\tau_c - 1}{\tau_f - 1}\left[f_i^{+,f} - f_i^{\mathrm{eq},f}\right]. \tag{14}$$

Similarly, when transferring the information from coarse block to fine block, the post-collision distribution function at nodes "●" can be calculated by [36]:

$$f_i^{+,f} = f_i^{\mathrm{eq},c} + \frac{\tau_f - 1}{m(\tau_c - 1)}\left[f_i^{+,c} - f_i^{\mathrm{eq},c}\right]. \tag{15}$$

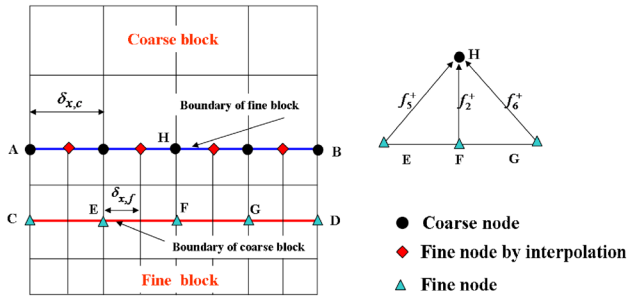

(a) Information exchange on interface of two blocks

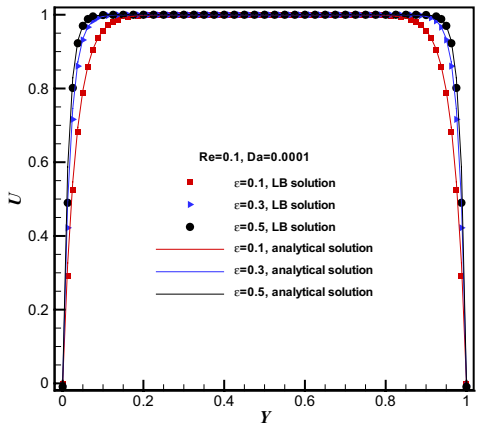

Velocity profile along *Y*-direction

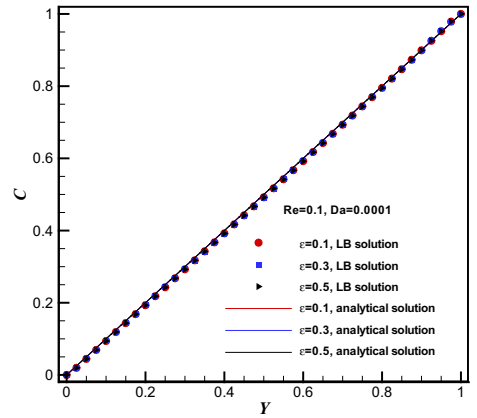

Concentration profile along *Y*-direction

(b) Velocity and concentration profiles along *Y*-direction at outlet

Fig. 1 **a** Information exchange on the interface of two blocks with various lattice densities. **b** Comparison of concentration and velocity profiles between LB results and analytical results for various porosities

On the boundary of fine block, the information at nodes "○" can be obtained with the information at nodes "●" by a symmetric cubic spline fitting [36]:

$$f^{+}(x) = a_i + b_i x + c_i x^2 + d_i x^3, x_{i-1} \le x \le x_i, i = 1, \ldots, m, \tag{16}$$

where a_i, b_i, c_i, d_i are determined by the continuity of the nodal conditions of f^{+}, $f^{+\prime}$, $f^{+\prime\prime}$ and suitable end condition.

To ensure the interface information at the correct time level, the temporal interpolation of three-point Lagrangian formation is needed. On the boundary $\overline{\mathrm{AB}}$, the post-collision distribution function $f_i^{+}(t+\delta_{t,f})$ can be calculated by the information at $t-\delta_{t,c}$, t and $t+\delta_{t,c}$:

$$f_i^{+,f}(t) = \sum_{k=1}^{3}\left(f_i^{+,f}(t_k)\prod_{\substack{j=1\\ j\neq k}}^{3}\frac{t-t_k}{t_k-t_j}\right). \tag{17}$$

3 Validation and simulation model

3.1 Validation of the model

In order to verify the LB model combined with a multi-block scheme, the flow and mass transfer is simulated for flow in a channel filled with porous media for $\varepsilon = 0.1$, 0.3 and 0.5. In LB simulation, the computational domain is divided into two parts, and the coarse and fine blocks are, respectively, implemented to the front and rear parts. The periodic boundary condition is employed at the inlet and outlet boundaries, and the velocity and concentration boundary conditions at the top and bottom walls are set as $U_{\mathrm{up}} = U_{\mathrm{bottom}} = 0.0$, $C_{\mathrm{up}} = 1.0$ and $C_{\mathrm{bottom}} = 0.0$.

As the Reynolds number (Re) and Da number are very small, the analytical solutions of velocity and concentration are described as $U = \frac{GK}{\nu}\left(1 - \frac{\cosh(r(Y-H/2))}{\cosh(rH/2)}\right)$ with $r = \sqrt{\nu\varepsilon/K\nu_e}$, and $C = \frac{C_{\mathrm{up}}-C_{\mathrm{bottom}}}{e^{UH/D_\sigma}-1}e^{UY/D_\sigma} + \frac{C_{\mathrm{bottom}}e^{UH/D_\sigma}-C_{\mathrm{up}}}{e^{uH/D_\sigma}-1}$. Figure 1b presents the velocity and concentration profiles along Y-direction at the outlet for various porosities at $Da = 0.0001$, $Re = 0.1$, showing an excellent agreement between the LB results and analytical solutions.

3.2 Simulation model

Figure 2 presents the wastewater solution with influent velocity u_0 and concentration c_0 passes over a circular optical fiber, where attaches uniform PSB biofilm with thickness of δ. The organic substance is delivered into the biofilm and subsequently biodegraded by bacteria, and simultaneously hydrogen is generated. In this work, the following assumptions are set as follows:

1. A steady-state uniform biofilm is formed on the surface of optical fiber.
2. The bioreaction operates in the optimum temperature (30 °C), pH (7.0) and illumination intensity (6000 lx), and the reaction system is implemented under a steady-state condition.

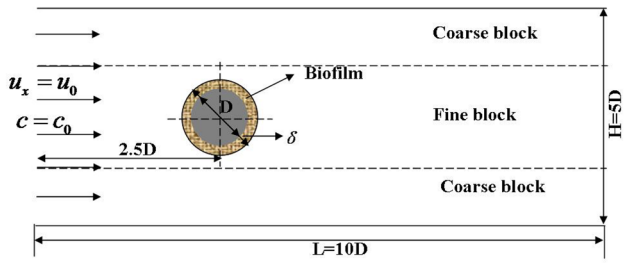

Fig. 2 Computational domain for solution flowing through PSB biofilm attached on a circular optical fiber

3. The substrate (glucose) and product (hydrogen) are completely dissolved in the solution, and thereby the reaction flow is considered as a single phase flow.

The substrate consumption rate r_1 and product generation rate r_2 by PSB (*Rhodopseudomonas palustris* CQK 01) in the biofilm are expressed by [39]

$$r_1 = \frac{1}{Y_{x/s}} \frac{\mu_{\max} c_1 C_x}{k_s + c_1} + mC_x, \quad r_2 = \alpha \frac{1}{Y_{x/s}} \frac{\mu_{\max} c_1 C_x}{k_s + c_1} + \beta C_x, \tag{18}$$

where C_x is the initial cell density, 0.76 kg m^{-3}; $Y_{x/s}$ the cell yield, 0.85; k_s the Monod constant, 5.204 kg m^{-3}; β is the reaction kinetic constant for hydrogen production, 0.41 h^{-1}. c_1 is the local substrate concentration. $\mu_{\max}$ denotes the maximum specific growth rate (h^{-1}), m the maintenance coefficient (h^{-1}), α is the reaction kinetic constant for hydrogen production at a given reaction condition (h^{-1}).

Convenient for generalization and analysis, normalizations are conducted using the optical fiber diameter d, inlet fluid velocity u_0 and inlet fluid concentration c_0, and a set of dimensionless variables is expressed as

$$X = x/d, \quad Y = y/d, \quad \mathbf{U} = \mathbf{u}/u_0, \quad C_\sigma = c_\sigma/c_0, \quad \mathrm{Re} = u_0 d/\nu. \tag{19}$$

In this study, the flow and mass transfer in the bioreactor are simulated with help of REV–LBM combined with multi-block scheme. As shown in Fig. 2, fine grids are implemented in central domain, and coarse grids are implemented in other two domains. The ratio of the lattice space between the two blocks is $m = 2$, and the fine and coarse grid mesh are set as $N_x \times N_y = 201 \times 41$ and $N_x \times N_y = 101 \times 15$, respectively. The boundary conditions are set as:

Inlet boundary: $U = U_0$, $C = C_0$

Upper and bottom boundaries: $\mathbf{U} = 1.0, \frac{\partial C}{\partial Y} = 0$

Curved boundary of optical fiber: $\mathbf{U} = 0.0, \frac{\partial C}{\partial \mathbf{n}} = 0$

Outlet boundary: $\frac{\partial \mathbf{U}}{\partial X} = 0, \quad \frac{\partial C}{\partial X} = 0.$

For boundary condition treatment in LB simulation, the non-equilibrium extrapolation method for plane and curved boundaries [40, 41] are, respectively, implemented to around boundaries and curved boundary of optical fiber. Furthermore, the bioreactor performance is assessed by substrate consumption efficiency η, which is defined as:

$$\eta = \left(\frac{m_{\text{in}} - m_{\text{out}}}{m_{\text{in}}} \right) \Big|_{\text{substrate}} \times 100\%. \tag{20}$$

4 Results and discussion

The biofilm directly influences fluid flow and mass transfer either in the domain flow or biofilm, and subsequently affects the biodegradation of substrate by PSB. Therefore, the characteristics of biofilm, as a porous media, are investigated to improve the photobioreactor performance.

4.1 Effect of porosity of biofilm

The porosity of porous media is an important parameter to measure the fraction of voids volume over the total volume, and the effect of porosity of biofilm is firstly studied. Figure 3a presents velocity fields (i.e., velocity magnitude) for solution past a circular optical fiber attached with PSB biofilm with various porosities at $Da = 0.001$. For all cases, higher fluid velocity appears at the top and bottom parts of biofilm. Comparing these flow fields with various porosities, $\varepsilon = 0.1$, 0.3 and 0.5, it can be obviously noticed from Fig. 3a that for lower porosity ($\varepsilon = 0.1$), the solution fluid passes through the PSB biofilm with a higher velocity. With increasing porosity, the fluid velocity decreases with a larger drop at the interface of main flow region and biofilm, and thereby the velocity gradient increases at the interface. Additionally, the region with lower velocity becomes larger with increasing porosity, particularly at the direction perpendicular to the fluid flow direction. More clearly, Fig. 3b compares the velocity profiles along Y-direction at rare of the circular optical fiber ($X = 15.5$) for various porosities. Obviously, the fluid velocity in the biofilm is fairly low compared with that in the main flow region, and it decreases with increasing porosity. However, it is opposite in main flow region.

Correspondingly, apparent effect of porosity on mass transport of substrate and product is found. Figure 4a, b present the concentration fields (i.e., concentration magnitude) of substrate and product for solution flowing through PSB biofilm attached on a circular optical fiber at $Da = 0.001$, corresponding to the flow fields in Fig. 3a. Under the condition of $\varepsilon = 0.1$, there are two small symmetric regions with maximum concentration of substrate in the biofilm, and lower concentration appears at the rear of the optical fiber, as shown in Fig. 4a. With the increase of porosity, these regions gradually become indistinct and the concentration distribution of substrate becomes more uniform in the biofilm. It also can be seen that the concentration of substrate is higher

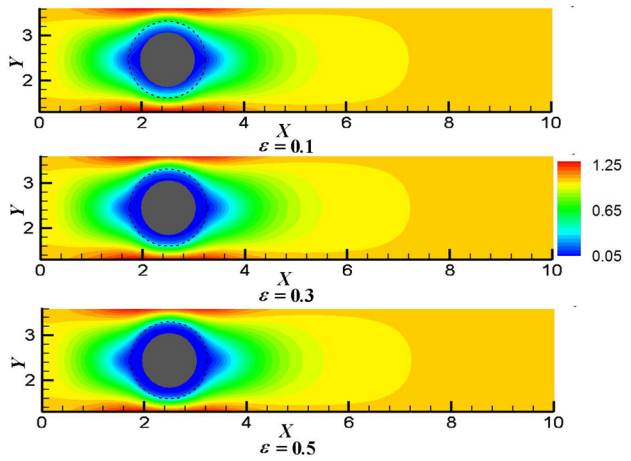

(a) Velocity fields

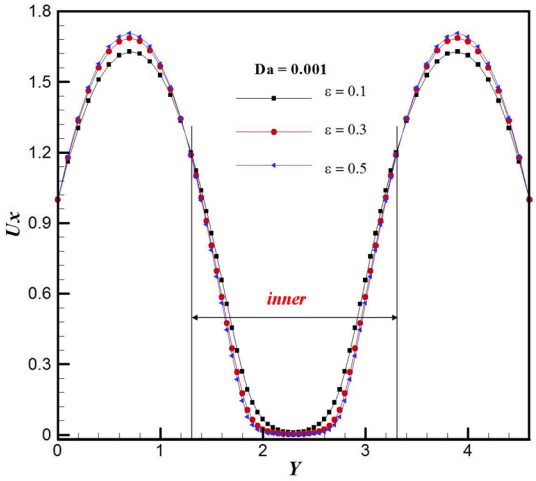

(b) velocity profiles along *Y*-direction at *X*=15.5

Fig. 3 Velocity fields and profiles for substrate solution flowing through PSB biofilm attached on a circular optical fiber for various porosities at $Da = 0.001$. **a** Velocity fields, **b** velocity profiles along *Y*-direction at $X = 15.5$

at the interface of biofilm for $\varepsilon = 0.1$, which is ascribed to the fact that the fluid flow with higher velocity carries more substrate load into the biofilm for biohydrogen production. As the generation of hydrogen product in the biofilm, the product concentration in the biofilm is higher than that in the main flow region, as shown in Fig. 4b. The maximum concentration appears at the rear part of biofilm and it decreases with increasing porosity. It is noted that the region with higher product concentration has a forward extension along the surface of optical fiber, while shrinks along flow direction, attributed to the impact of flow fields. Additionally, the concentration boundary layer becomes thicker for larger porosity, due to weaker convection for lower velocity.

To better understand the mass transfer, Fig. 4c, d present the concentration profiles of substrate and product along *Y*-direction at $X = 15.5$ for various porosities of biofilm. The variation of concentration is significant in the biofilm, both for substrate and product. Deeper into the biofilm, the concentration varies more dramatically, particularly for substrate (Fig. 4c), implying that the concentration gradient increases. With the increasing of porosity, the concentration of substrate decreases at the rear of optical fiber, while the concentration of product increases near the surface of biofilm and then decreases deeper into the biofilm in Fig. 4d, which is attributed to the region with higher concentration of product at the rear of optical fiber.

4.2 Effect of permeability of biofilm

The parameter of permeability *K* is important to measure the ability of porous media to transmit fluid, and it is represented by a dimensionless parameter of Darcy number, *Da*. Large *Da* number corresponds to strong penetrability of porous media. Figure 5a describes the velocity fields for solution fluid flowing through the biofilm attached on a circular optical fiber for various *Da* numbers at $\varepsilon = 0.3$. When fluid flows from main flow region into biofilm, the velocity decreases dramatically, particularly for low *Da* number, cf. $Da = 0.0001$. This is ascribed to high flow resistance in biofilm leading to great pressure loss. With the increase of *Da* number, fluid velocity obviously increases in the biofilm, and the region with low velocity sharply shrinks, particularly at the direction perpendicular to flow direction. It can be understood that larger Darcy number leads to higher permeability, and thereby fluid easily flows through into the biofilm with lower flow resistance. Additionally, one can obviously notice that the velocity boundary layer on the biofilm becomes thinner with the increase of *Da* number, resulting from greater velocity gradient at the interface. For more clarity, Fig. 5b presents the velocity profiles along *Y*-direction at $X = 15.5$ for $\varepsilon = 0.3$. For a larger *Da* number, cf. $Da = 0.005$, the solution has a lower velocity in the main flow region, while the fluid velocity is higher in biofilm and approximates a standard parabolic profile.

As hydrodynamics and mass transfer are coupled closely, therefore the impacts on mass transfer combined bioreaction are investigated. Figure 6a, b present the concentration of substrate and product for solution flowing through PSB biofilm attached on a circular optical fiber. It can be seen in Fig. 6a that the substrate concentration is fairly lower in biofilm, compared with that in main flow region. In the rear part of biofilm, the concentration of substrate is lower than that in the front part of biofilm. This can be understood that fewer substrate loads are delivered into biofilm in the wake region with lower velocity, and simultaneously lower velocity prolongs hydraulic retention time (HRT) for sufficient biodegradation in biofilm, and thereby the concentration of substrate is lower in the rear part of biofilm.

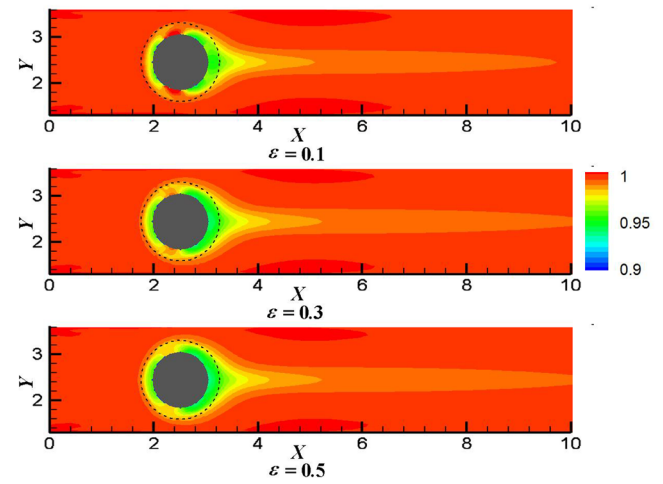

(a) substrate concentration fields

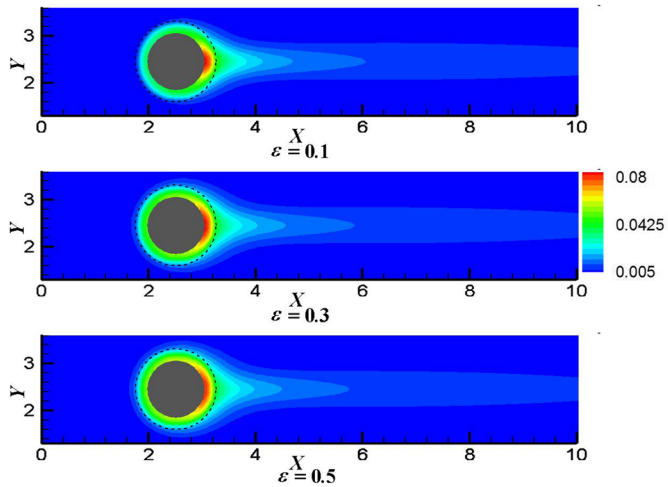

(b) product concentration fields

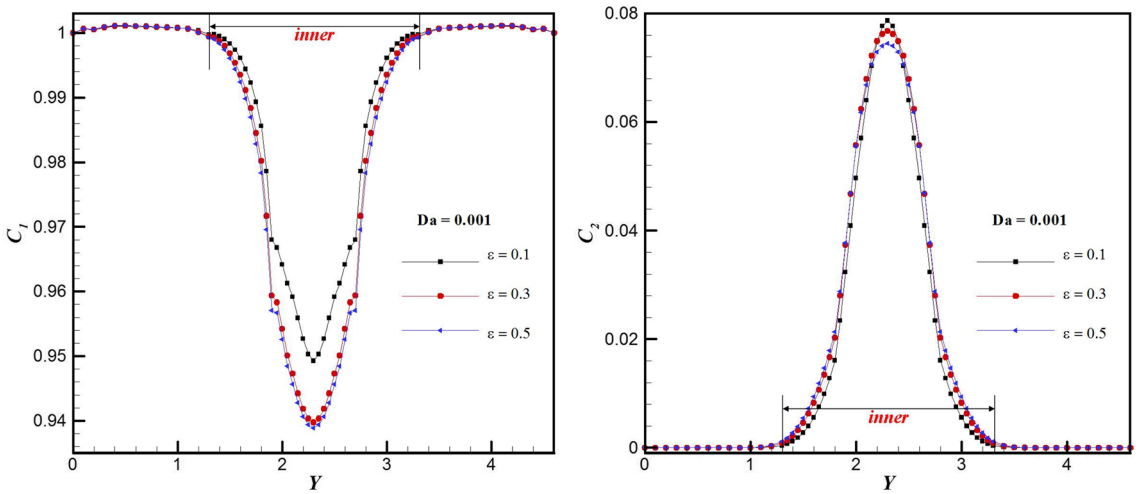

(c) substrate concentration profiles

(d) product concentration profiles

Fig. 4 Concentration fields and profiles along *Y*-direction at $X = 15.5$ for substrate solution flowing through PSB biofilm attached on a circular optical fiber for various porosities at $Da = 0.001$. **a** Substrate concentration fields, **b** product concentration fields, **c** substrate concentration profiles and **d** product concentration profiles along *Y*-direction at $X = 15.5$

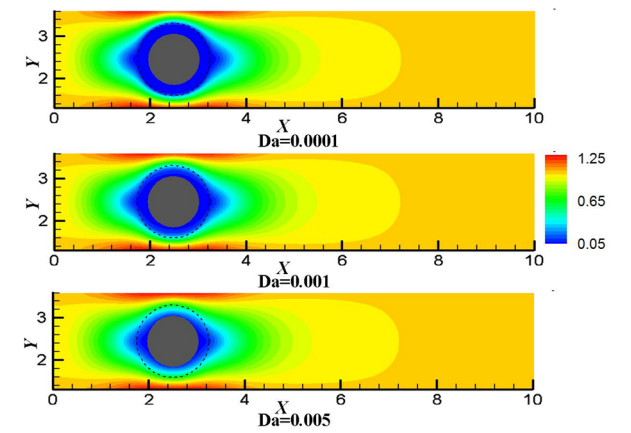

(a) velocity fields

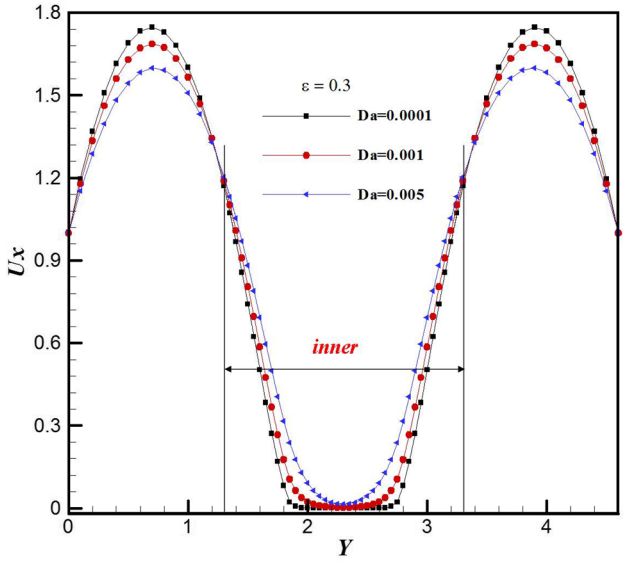

(b) velocity profiles along *Y*-direction at *X*=15.5

Fig. 5 Velocity fields and profiles along *Y*-direction at $X=15.5$ for substrate solution flowing through PSB biofilm attached on a circular optical fiber for various *Da* numbers at $\varepsilon=0.3$. **a** Velocity fields, **b** velocity profiles along *Y*-direction at $X=15.5$

Since the impact of flow field, two regions with maximum concentration of substrate appear in the front part of biofilm, and the regions become more apparent for a larger *Da* number. With increasing *Da* number, the concentration of substrate increases in biofilm, which mainly ascribed to the fact that the fluid carries more substrate loads into the biofilm with a higher velocity. However, high velocity shortens HRT, and thus there is insufficient time for biodegradation of substrate even though enhancing the mass transport. Figure 6b shows that the region with maximum concentration of product appears in the rear part of biofilm, and the region significantly shrinks backward along the surface of optical fiber for a large *Da* number. This is because that the flow resistance decreases and velocity increases with the increase of *Da* number, and more product generated in the biofilm are carried backwards by fluid flow with high velocity. The concentration boundary layer becomes thinner with increasing *Da* number, both for substrate and product (cf. Fig. 6a, b), due to the influence of flow fields (cf. Fig. 5). For more clarity, Fig. 6c, d present the concentration profiles of substrate and product along *Y*-direction at $X=15.5$. It is noted that two symmetric break points of substrate concentration appear in biofilm at the rear of optical fiber in Fig. 6c. The product concentration increases deeper into the biofilm in Fig. 6d, which can be understood that the product generated in biofilm is transferred outwards and downstream by fluid flow, leading to a concentration gradient of product in biofilm. As the variation of maximum concentration region at the rear part of biofilm, the concentration profiles of product are different, and the concentration deeper into the biofilm is highest for $Da=0.001$, and that for $Da=0.0001$ is lowest.

4.3 Biodegradation performance

Besides investigation of hydrodynamics and mass transfer associated with bioreaction, the biodegradation performance is evaluated as well, by substrate consumption efficiency η. Table 1 presents the substrate consumption for substrate solution through PSB biofilm attached on a circular optical fiber. It is noted that the LB results have a good agreement with the experimental data [42], proving the feasibility of the LB model for porous media. The LB numerical result shows that for a given porosity, the substrate consumption efficiency increases with increasing *Da* number and achieves maximum at $Da=0.001$, while it decreases for further increasing *Da* number. This can be attributed to the fact that more substrate load is supplied for sufficient biodegradation in biofilm with increasing *Da* number, and then it leads to the improvement of substrate consumption efficiency. However, for further increasing *Da* number, increment of substrate load delivered by solution exceeds the consumption of PSB and the inhibition of substrate for high concentration appears. Meanwhile, the increase of fluid velocity for larger *Da* number obviously shortens HRT, and then there is not enough time for sufficient bioreaction, thereby decreasing the substrate consumption efficiency. However, for a given *Da* number, the variation of substrate consumption efficiency is different. For example, when $Da=0.0001$, the substrate consumption efficiency achieves maximum at $\varepsilon=0.1$, while for $Da=0.001$ and 0.005, that gets maximum at $\varepsilon=0.3$ and $\varepsilon=0.5$, respectively. This implies that the biodegradation performance is affected by both porosity and Darcy number. Comparing all cases in Table 1, it can be seen that the substrate consumption efficiency is lowest for the condition of $Da=0.005$ and $\varepsilon=0.1$. This is ascribed to the fact that the lower porosity and larger *Da* number lead

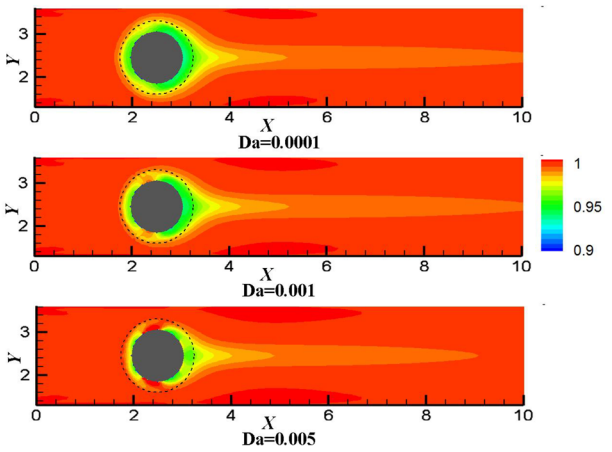

(a) Substrate concentration fields

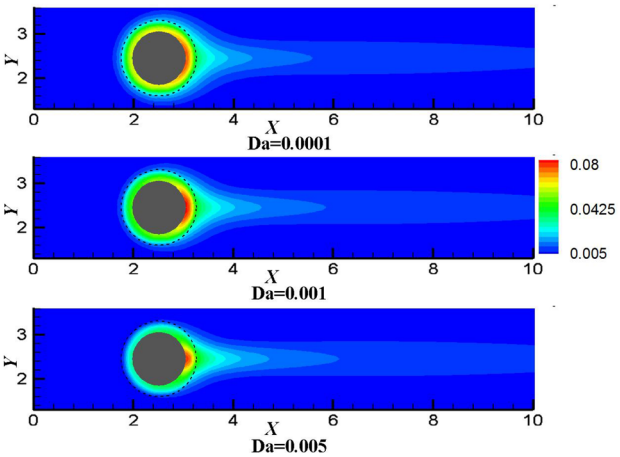

(b) Product concentration fields

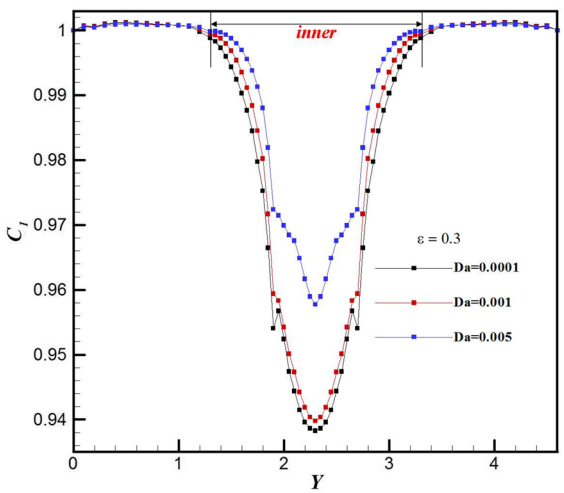

(c) substrate concentration profiles

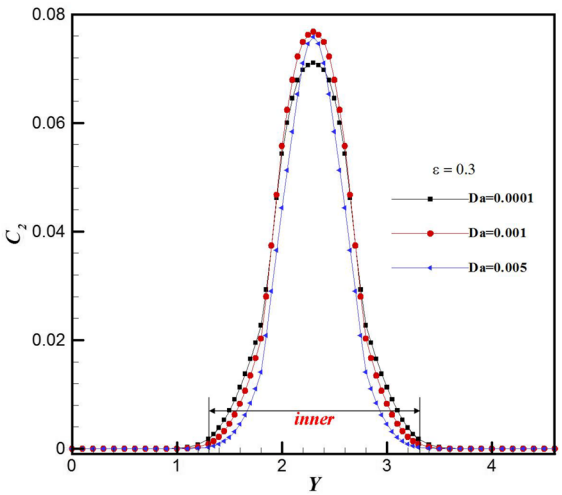

(d) product concentration profiles

Fig. 6 Concentration fields and profiles along Y-direction at $X = 15.5$ for substrate solution flowing through PSB biofilm attached on a circular optical fiber for various Da numbers at $\varepsilon = 0.3$. **a** Substrate concentration fields, **b** product concentration fields, **c** substrate concentration profiles and **d** product concentration profiles along Y-direction at $X = 15.5$

Table 1 Substrate consumption efficiency for substrate solution flowing through PSB biofilm attached on a circular optical fiber

η/%	LB results			Experimental data [42]
	$Da = 0.0001$	$Da = 0.001$	Da = 0.005	
$\varepsilon = 0.1$	4.98	5.04	3.80	
$\varepsilon = 0.3$	4.92	5.13	4.80	4.85 – 4.93
$\varepsilon = 0.5$	4.90	5.07	5.06	

to a higher fluid velocity in the biofilm. The higher fluid velocity accelerates the mass transport between the bulk flow and biofilm, and supplies amount of substrate load for biodegradation by microorganisms, which causes inhibition effect from high substrate concentration and reduction of metabolic activity of PSB. As analyzed above, the higher fluid velocity shortens HRT for bioreaction of PSB. Therefore, the substrate consumption efficiency is lowest under the condition of $Da = 0.005$ and $\varepsilon = 0.1$. While it is highest under the condition of $Da = 0.001$ and $\varepsilon = 0.3$, implying that this suitable condition facilitates the transport of substrate and product, and enhances the metabolic activity of bacteria in biofilm.

5 Conclusion

The mechanisms of hydrodynamics and mass transfer are investigated for substrate solution flowing through PSB biofilm attached on a circular optical fiber with lattice Boltzmann method. A multi-block scheme is coupled with the lattice Boltzmann model for the sake of high computational efficiency and accuracy. The flow and concentration fields are plotted, and the effects of porosity and permeability of biofilm on hydrodynamics and mass transport are analyzed. The result shows that the region with minimum substrate concentration and maximum product concentration appears at the rear part of biofilm, and the region obviously extends forward along the surface of optical fiber with increasing porosity, while it shrinks backward with increasing Da number. Furthermore, the biodegradation performance is evaluated by substrate consumption efficiency. It is demonstrated that the optimal biodegradation performance is obtained for $Da = 0.001$ and $\varepsilon = 0.3$, because the characteristic of biofilm facilitates the mass transport of substance and the metabolic activity of PSB. However, the substrate consumption efficiency is lowest for $Da = 0.005$ and $\varepsilon = 0.1$, ascribed to the inhibition effect of substrate for high concentration and the reduction of metabolic activity of bacteria in biofilm, as well as shorter HRT for bioreaction. Furthermore, the LB numerical results have a good agreement with the experimental results, which proves the feasibility of the LB model for bioreaction.

Acknowledgements The authors are grateful for the financial support provided by the National Natural Science Foundation of China (51506139) and the Key Laboratory of Low-grade Energy Utilization Technologies and Systems Foundation (LLEUTS-201607).

References

1. G.P. Sheng, H.Q. Yu, X.Y. Li, Extracellular polymeric substances (EPS) of microbial aggregates in biological wastewater treatment systems: a review. Biotechnol. Adv. **28**(6), 882–894 (2010)
2. A. Shojaie, M. Fattahi, S. Jorfi, B. Roozbehani, Hydrothermal synthesis of Fe–TiO_2–Ag nano-sphere for photocatalytic degradation of 4-chlorophenol (4-CP): investigating the effect of hydrothermal temperature and time as well as calcination temperature. J. Environ. Chem. Eng. **5**(5), 4564–4572 (2017)
3. A. Payan, M. Fattahi, S. Jorfi, B. Roozbehani, S. Payan, Synthesis and characterization of titanate nanotube/single-walled carbon nanotube (TNT/SWCNT) porous nanocomposite and its photocatalytic activity on 4-chlorophenol degradation under UV and solar irradiation. Appl. Surf. Sci. **434**, 336–350 (2018)
4. S.Z. Shirejini, M. Fattahi, Mathematical modeling and analytical solution of two-phase flow transport in an immobilized-cell photobioreactor through the homotopy perturbation method (HPM). Int. J. Hydrogen Energy **41**(41), 18405–18417 (2016)
5. C.S. Butler, J.P. Boltz, *3.6-Biofilm Processes and Control in Water and Wastewater Treatment*, in *Comprehensive Water Quality and Purification*, ed. by S. Ahuja, (Elsevier, Waltham, 2014), pp. 90–107
6. G. Kars, U. Gündüz, Towards a super H2 producer: improvements in photofermentative biohydrogen production by genetic manipulations. Int. J. Hydrogen Energy **35**(13), 6646–6656 (2010)
7. J. Cheng, L.K. Ding, R.C. Lin, L.C. Yue, J.Z. Liu, J.H. Zhou, K.F. Cen, Fermentative biohydrogen and biomethane co-production from mixture of food waste and sewage sludge: effects of physiochemical properties and mix ratios on fermentation performance. Appl. Energy **184**, 1–8 (2016)
8. R.K. Goud, K. Arunasri, D.K. Yeruva, K.V. Krishna, S. Dahiya, S.V. Mohan, Impact of selectively enriched microbial communities on long-term fermentative biohydrogen production. Bioresour. Technol. **242**, 253–264 (2017)
9. V. Maria, C. Blanco, L.T. Fuess, M. Zaiat, Calcium dosing for the simultaneous control of biomass retention and the enhancement of fermentative biohydrogen production in an innovative fixed-film bioreactor. Int. J. Hydrogen Energy **42**(17), 12181–12196 (2017)
10. V. Gadhamshetty, A. Sukumaran, N. Nirmalakhandan, M.T. Myint, Photofermentation of malate for biohydrogen production—a modeling approach. Int. J. Hydrogen Energy **33**(9), 2138–2146 (2008)
11. S.J. Wang, Z.H. Ma, T. Zhang, M.D. Bao, H.J. Su, Optimization and modeling of biohydrogen production by mixed bacterial cultures from raw cassava starch. Front. Chem. Sci. Eng. **11**(1), 100–106 (2017)
12. X. Wang, J. Ding, W.Q. Guo, N.Q. Ren, Scale-up and optimization of biohydrogen production reactor from laboratory-scale to industrial-scale on the basis of computational fluid dynamics simulation. Int. J. Hydrogen Energy **35**(20), 10960–10966 (2010)
13. Q. Liao, D.M. Liu, D.D. Ye, X. Zhu, D.J. Lee, Mathematical modeling of two-phase flow and transport in an immobilized-cell photobioreactor. Int. J. Hydrogen Energy **36**(21), 13939–13948 (2011)

14. S. Chen, G.D. Doolen, Lattice Boltzmann method for fluid flows. Annu. Rev. Fluid Mech. **30**(1), 329–364 (1998)
15. X. He, L.S. Luo, Theory of the lattice Boltzmann method: from the Boltzmann equation to the lattice Boltzmann equation. Phys. Rev. E **56**(6), 6811 (1997)
16. S. Chen, D. Martinez, R. Mei, On boundary conditions in lattice Boltzmann methods. Phys. Fluids **8**(9), 2527–2536 (1996)
17. Z.L. Guo, B.C. Shi, N.C. Wang, Lattice BGK model for incompressible Navier–Stokes equation. J. Comput. Phys. **165**(1), 288–306 (2000)
18. Y.H. Qian, D. d'Humieres, P. Lallemand, Lattice BGK models for Navier–Stokes equation. Europhys. Lett. **17**(6), 479–484 (1992)
19. B. Chopard, P.O. Luthi, Lattice Boltzmann computations and applications to physics. Theor. Comput. Sci. **217**(1), 115–130 (1999)
20. S. Succi, *The lattice Boltzmann equation For Fluid Dynamics and Beyond* (Oxford University Press, Oxford, 2001)
21. L. Biferale, P. Perlekar, M. Sbragaglia, F. Toschi, Convection in multiphase fluid flows using lattice Boltzmann methods. Phys. Rev. Lett. **108**(10), 104502 (2012)
22. S.H. Kim, H. Pitsch, I.D. Boyd, Lattice Boltzmann modeling of multicomponent diffusion in narrow channels. Phys. Rev. E **79**(1), 016702 (2009)
23. J. Onishi, Y. Chen, H. Ohashi, Dynamic simulation of multi-component viscoelastic fluids using the lattice Boltzmann method. Phys. A Stat. Mech. Appl. **362**(1), 84–92 (2006)
24. C. Xie, J. Zhang, M. Wang, Lattice Boltzmann modeling of non-Newtonian multiphase fluid displacement. Chin. J. Comput. Phys. **33**(2), 147–155 (2016)
25. H. Paradis, M. Andersson, B. Sunden, Modeling of mass and charge transport in a solid oxide fuel cell anode structure by a 3D lattice Boltzmann approach. Heat Mass Transf. **52**(8), 1529–1540 (2016)
26. Y. Gao, X. Zhang, P. Rama, Y. Liu, R. Chen, H. Ostadi, K. Jiang, Calculating the anisotropic permeability of porous media using the lattice Boltzmann method and X-ray computed tomography. Transp. Porous Med. **92**(2), 457–472 (2012)
27. N. Verma, D. Mewes, Lattice Boltzmann methods for simulation of micro and macrotransport in a packed bed of porous adsorbents under non-isothermal condition. Comput. Math. Appl. **58**(5), 1003–1014 (2009)
28. K. Yamamoto, N. Takada, M. Misawa, Combustion simulation with Lattice Boltzmann method in a three-dimensional porous structure. Proc. Combust. Inst. **30**(1), 1509–1515 (2005)
29. T. Wang, Q. Gao, J. Chen, H. Xu, M. Yang, Lattice Boltzmann simulation of mixed convection in an enclosure filled with porous medium. Chin. J. Comput. Phys. **34**(1), 39–46 (2017)
30. M. Raúl, Numerical simulations of surface reaction in porous media with lattice Boltzmann. Chem. Eng. Sci. **69**(1), 628–643 (2012)
31. T. Lei, X. Meng, Z. Guo, Lattice Boltzmann study on influence of chemical reaction on mixing of miscible fluids with viscous instability in porous media. Chin. J. Comput. Phys. **33**(4), 399–409 (2016)
32. L.K. Li, C. Chen, A. Singh, N. Rahmatian, N. AuYeung, K. Randhir, R.W. Mei, J.F. Klausner, D.W. Hahn, J. Petrasch, A transient heat transfer model for high temperature solar thermochemical reactors. Int. J. Hydrogen Energy **41**(4), 2307–2325 (2016)
33. S.P. Sullivan, F.M. Sani, M.L. Johns, L.F. Gladden, Simulation of packed bed reactors using lattice Boltzmann methods. Chem. Eng. Sci. **60**(12), 3405–3418 (2005)
34. Z.L. Guo, T.S. Zhao, Lattice Boltzmann model for incompressible flows through porous media. Phys. Rev. E **66**(3), 036304 (2002)
35. P. Nithiarasu, K.N. Seetharamu, Natural convection heat transfer in a fluid saturated variable porosity medium. Int. J. Heat Mass Transf. **40**, 3955–3967 (1997)
36. D.Z. Yu, R.W. Mei, W. Shyy, A multi-block lattice Boltzmann method for viscous fluid flows. Int. J. Numer. Methods Fluids **39**(2), 99–120 (2002)
37. S. Ergun, Fluid flow through packed columns. Chem. Eng. Prog. **48**, 89–94 (1952)
38. K. Vafai, Convective flow and heat transfer in variable porosity media. J. Fluid Mech. **147**, 233–259 (1984)
39. D. Liu, *Modeling for Multiphase Flow and Transport with Biochemical Reaction in Immobilized Photobioreactor for Hydrogen Production*, (Chongqing University, Chongqing, 2010)
40. Z.L. Guo, C.G. Zheng, B.C. Shi, An extrapolation method for boundary conditions in lattice Boltzmann method. Phys. Fluids **14**(6), 2007–2010 (2002)
41. Q. Zou, X. He, On pressure and velocity boundary conditions for the lattice Boltzmann BGK model. Phys. Fluids **9**(6), 1591–1598 (1997)
42. G. Chenglong, *Transport Characteristics in Biofilm Photobioreactor with Photosynthetic Bacteria and Enhancement of Hydrogen Production Performance* (Chongqing University, Chongqing, 2013)